Strengthening mechanisms in a Zr-modified 5083 alloy deformed to high strains

2 authors:

S. S. Malopheyev
Belgorod State University
33 PUBLICATIONS   **123** CITATIONS

SEE PROFILE

Rustam Kaibyshev
Belgorod State University
418 PUBLICATIONS   **4,384** CITATIONS

SEE PROFILE

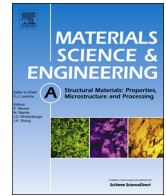Some of the authors of this publication are also working on these related projects:

Development of high-Mn austenitic steels with improved fatigue properties View project

Design and development of new creep-resistant chromium steels for USC boilers and steam lines and theirs manufacturing technologies. View project

Strengthening mechanisms in a Zr-modified 5083 alloy deformed to high strains

CrossMark

S. Malopheyev *, R. Kaibyshev

Belgorod State University, Pobeda 85, Belgorod 308015, Russia

ABSTRACT

The effect of extensive grain refinement through equal-channel angular processing (ECAP) at 300 °C on the mechanical properties was examined in a Zr-modified 5083 aluminum alloy. It was shown that any increase in the yield stress (YS) by increasing the number of pressings was attributed to additional contributions from three strengthening mechanisms: (i) grain boundary strengthening related to the size of the crystallites bounded by deformation-induced high-angle boundaries (HAB), (ii) dislocation strengthening related to highly increased dislocation density and (iii) solute strengthening related to promoting dynamic strain aging (DSA) by intense plastic straining. Grain size strengthening is the primary contributor to the increase in the YS as a result of ECAP. Dislocation strengthening plays an important but minor role in strengthening the alloy after ECAP. No ECAP effect on the dispersion strengthening was observed. However, a dispersion of nanoparticles was found to cause an increase in the YS through grain refinement and the accumulation of lattice dislocations during ECAP. It was found that the deformation-induced low angle boundaries (LABs) play an insignificant role in the strengthening of the material.

© 2014 Elsevier B.V. All rights reserved.

1. Introduction

Non-age-hardenable Al–Mg alloys are widely used due to their good weldability, ductility, toughness, formability and high levels of corrosion resistance [1]. However, annealed versions of these alloys exhibit low yield stresses (YS) ranging from 90 to 160 MPa, depending on the Mg content [1,2]. Al–Mg alloys can be strengthened by cold working, which results in a significant increase to the YS and the ultimate tensile strength (UTS), by as much as a factor of 1.5–3 [1,2]. Increasing the Mg content enhances the efficiency of the strain hardening process, and Al–6% Mg alloys have been shown to exhibit a YS exceeding 400 MPa in a fully hardened condition [1,2]. However, any increase in the YS due to strain hardening is obtained at the expense of ductility [1]. The other approach taken to increase the strength of Al–Mg alloys and retain essential ductility consists of forming ultra-fine grained (UFG) structures using equal-channel angular pressing (ECAP) [3–9]. YS and UTS values of approximately 400 and 420 MPa, respectively, along with a ductility of ∼9% can be attained in 5XXX series aluminum alloys with Mg contents ranging from 1.5% to 3% using

ECAP to an effective strain of ∼8 at temperatures ranging from 20 to 200 °C [3–9]. This processing is more effective compared to convention strain hardening and may provide a 50% increase to the YS and UTS compared to coarse grained (CG) reference materials with an H38 (full hardening and final stabilization at ∼140 °C) temper [6].

The origin of the increased strength in materials with an UFG structure as a result of ECAP is still a subject of debate. It was assumed [10,11] that this increase could be attributed to grain size strengthening via the well-known Hall–Petch relationship [1,2]:

$$\sigma_y = \sigma_0 + k_y d^{-1/2}, \tag{1}$$

where σ_0 and k_y are experimentally determined constants. However, for Al–Mg alloys, the Hall–Petch slope for the YS ranges from 0.15 to 0.26 MPa m$^{1/2}$ and is dependent on the Mg and Mn contents [12,13]. This value is slightly higher than for aluminum and other aluminum alloys, in which k_y typically ranges from 0.06 to 0.15 MPa m$^{1/2}$, but is much smaller than observed in steels. Thus, grain size strengthening in Al–Mg alloys is not very efficiency. Therefore, extensive grain refinement cannot provide substantial increases to the YS [3–9]. A very high YS ranging from 750 to 900 MPa was recently attained in Al–Mg alloys through high pressure torsion by achieving a grain size of ∼100 nm [14,15]. These high YS values strongly deviate from the traditional Hall–Petch relationship (Eq. (1)). The authors [14] suggest an alternative

explanation for the effect of the grain size on the YS in an Al–Mg–Sc alloy. It is worth noting that ECAP performed at $T \leq 200$ °C leads to a reduction in the ductility [5–9], which is generally less than that observed when using such techniques as rolling, which is commonly employed to process hardened Al–Mg alloys [1,2,4].

The formation of UFG structures in Al–Mg alloys through intense plastic straining is accompanied by several processes in addition to grain refinement [3,4,16–18]. First, a many-fold increase in the lattice dislocation density takes place [5–9,16]. However, few attempts have been made to explain the high YS in Al–Mg alloys subjected to ECAP by examining the role of deformation strengthening. This may be attributed to the fact that experimental evaluations into the dislocation density for UFG structures are very limited [9] and, moreover, have been performed using X-ray techniques. It is apparent that the estimation of the effect of grain size on the YS in Al–Mg alloys containing dislocations densities greater than $\rho \sim 10^{14}$ m^{-2} without the contribution of deformation strengthening provides an overestimation of the k_y value. Secondly, the inspection of the experimental data [5,6,16,17] shows that the deformation structure consists mainly of elongated domains that are entirely or partially delimited by low-angle boundaries (LABs) and, therefore, are not considered to be grain boundaries [19,20]. Limited grain boundary statistics are available for Al–Mg alloys in which the Hall–Petch relationship was examined [16]. Thus pure information on the dislocation density and misorientations of deformation-induced boundaries preclude the interpretation of the high strength in Al–Mg alloys subjected to ECAP in terms of the additive contribution of the grain size strengthening and dislocation strengthening where the role of dislocation density stored in LABs was taken into account [11,21].

The main aim of this work is to analyze the strengthening mechanisms in an Al–Mg–Zr alloy subjected to ECAP at 300 °C. The dislocation structure and grain boundary statistics of this alloy are reported in a companion article [18] in greater detail. This article focuses on the effect of ECAP on the mechanical properties. The second goal of this study is to reveal the role of second phase particles in the strengthening resulting from intense plastic straining. For this purpose, the effect of ECAP on the mechanical properties was considered for a Zr-modified AA5083 alloy in two different conditions distinguished by different dispersions of the Al_6Mn phase.

2. Experimental

A Zr-modified commercial AA5083 alloy with a chemical composition of Al–5.4% Mg–0.5% Mn–0.1% Zr–0.12% Si–0.014% Fe (wt%) was fabricated by direct chill casting with a solidification rate of 100 K/s [18]. The ingots were then subjected to a homogenization annealing (HA) treatment at 360 °C for 6 h [18] with the final alloy designated as AA5083ZrHA1. Half of the solution treated samples were annealed again at 500 °C for 12 h [18]. This alloy was designated as AA5083ZrHA2. Next, both ingots were machined into billets with a square cross-section of 20×20 mm^2 and 100 mm in length. These billets were subjected to ECAP at ~ 300 °C for true strains of ~ 1, 2, 4, 8 and 12 via route B_C [4], at which a sample is rotated by 90° between each passes around pressing direction. The isothermal ECAP die had a square cross-section of 20×20 mm^2 and intersection angle of 90°. The pressing speed was ~ 3 mm/s. Finally, the pressed samples were water quenched.

The tensile tests at room temperature were conducted at a constant crosshead velocity corresponding to a nominal strain rate of 10^{-3} s^{-1} using an Instron 5882 universal testing machine.

Tensile samples with a 35 mm gauge length and a 7×3 mm^2 cross-sectional area were cut along the pressing direction. These specimen surfaces were mechanically polished to prevent the formation of surface defects and to achieve a uniform thickness. The fracture surfaces were examined using an FEI Quanta 200 3D scanning electron microscope. Other material and processing details were reported in previous work [18].

3. Results

3.1. Deformation structure

ECAP of the alloy led to the formation of new fine grains [18]. Deformation structures in two material conditions were distinctly different. At $\varepsilon \sim 12$, in the AA5083ZrHA1 alloy, the fully recrystallized structure consisted of ultra-fine grains with an average size of ~ 0.95 μm, while in the AA5083ZrHA2, recrystallized structure consisted of fine grains with an average size of ~ 1 μm and coarse grains with an average size of ~ 4 μm. Tables 1 and 2 summarize the microstructural characteristics of the AA5083Zr alloy over two conditions [18]. The main difference in the distribution of the secondary-phase particles between the two material conditions are the dispersion of the Al_6Mn phase [18]. In the AA5083ZrHA1 alloy, the secondary-phase particles have an average diameter of ~ 25 nm and the Zr is retained within the supersaturated solid solution [18]. The AA5083ZrHA2 alloy contains coarse, plate-like Al_6Mn particles with average dimensions of ~ 150 nm and ~ 60 nm in the longitudinal and transversal directions, respectively [18].

3.2. Mechanical properties

The engineering stress–strain curves for the AA5083Zr alloy, including the YS ($\sigma_{0.2}$), UTS (σ_B) and total elongation-to-failure (δ) are presented in Fig. 1 and Tables 3 and 4. The flow stress tends to increase and the strain hardening decreases with an increasing number of pressings for both material conditions (as seen in Fig. 1 and Tables 3 and 4). However, even at $\varepsilon \sim 12$, strain hardening

Table 1
Microstructural characteristics of the AA5083ZrHA1.

Material condition	Mean diameter of Al_6Mn particles (nm)	Volume fraction of Al_6Mn particles (%)	Boundary distance (μm)	Dislocation density (m^{-2})
HA1	25	2.5	250	10^{12}
ECAP 1 pass	25	2.5	**135** (5.8)	1.3×10^{14}
ECAP 2 passes	24	2.5	**63** (4)	1.2×10^{14}
ECAP 4 passes	24	2.5	**17** (1.5)	1.5×10^{14}
ECAP 8 passes	22	2.5	**3** (1.2)	8×10^{13}
ECAP 12 passes	22	2.5	**1.5** (1)	7.7×10^{13}

Table 2
Microstructural characteristics of the AA5083ZrHA2.

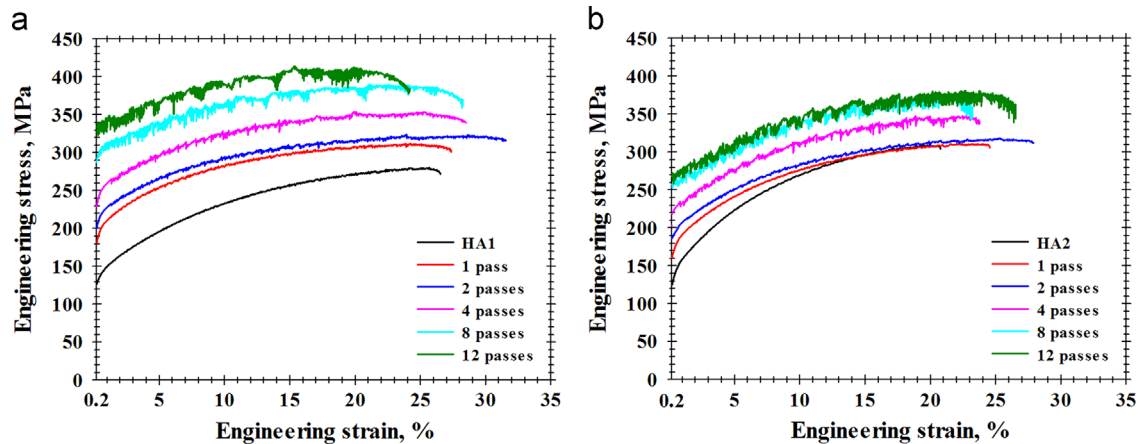| Material condition	Mean diameter of Al_6Mn particles (nm)	Volume fraction of Al_6Mn particles (%)	Boundary distance (μm)	Dislocation density (m^{-2})
HA1	100	2.5	250	10^{12}
ECAP 1 pass	100	2.5	**136** (6)	4.9×10^{13}
ECAP 2 passes	100	2.5	**57** (6.6)	4.6×10^{13}
ECAP 4 passes	100	2.5	**26** (2)	3.9×10^{13}
ECAP 8 passes	100	2.5	**7** (1.8)	3.8×10^{13}
ECAP 12 passes	100	2.5	**3.6** (2)	3.8×10^{13}

Fig. 1. Typical deformation diagrams for (a) the AA5083ZrHA1 and (b) the AA5083ZrHA2 under different conditions.

Table 3
Mechanical properties of the AA5083ZrHA1.

Material condition	Tensile properties in the pressing direction		
	Yield stress (MPa)	Ultimate tensile strength (MPa)	Ductility (%)
HA1	125	280	27
ECAP 1 pass	180	310	28
ECAP 2 passes	200	325	32
ECAP 4 passes	230	355	29
ECAP 8 passes	285	390	28
ECAP 12 passes	335	415	24

Table 4
Mechanical properties of the AA5083ZrHA2.

Material condition	Tensile properties in the pressing direction		
	Yield stress (MPa)	Ultimate tensile strength (MPa)	Ductility (%)
HA2	125	310	21
ECAP 1 pass	160	310	24
ECAP 2 passes	185	320	28
ECAP 4 passes	220	345	24
ECAP 8 passes	255	375	23
ECAP 12 passes	270	380	26

(represented by the UTS/YS ratio, as seen in Tables 3 and 4) is retained at sufficiently high levels to prevent instability in the plastic flow. As a result, the alloy exhibits high ductility after intense plastic straining over all the conditions (see Fig. 1 and Tables 3 and 4). In the initial condition, the YS in the both material conditions were the same. For the AA5083ZrHA1 alloy, the increases to both the YS and UTS values were higher after all passes than for the AA5083ZrHA2 alloy (see Tables 3 and 4). Therefore, the hardening of the AA5083Zr alloy containing a dispersion of round nanoparticles of the Al_6Mn phase subjected to ECAP is more effective than for the alloy containing coarser, plate-like Al_6Mn phase particles.

The transition from smooth to serrated flow via repeating oscillations in the stress–strain curves took place as the number of ECAP passes increased (see Fig. 1). The jerky flow phenomenon is generally associated with the Portevin-Le Chatelier (PLC) effect that is attributed to dynamic strain aging (DSA) [22–26]. After a second pressing, the so-called type A serrations were distinguished as an abrupt rise in the stress followed by a drop to or a drop below the general level of flow stress on the σ–ε curves for both material conditions. The critical strain, at which the serrations on the stress–strain curve appear [23–26], decreases with the strain. At $\varepsilon \geq 4$, jerky flow takes place immediately after reaching the yield point (see Fig. 1). In addition, the gradual transition from type A to the complex types C+A and A+B took place in the AA5083ZrHA1 and AA5083ZrHA2 alloys, respectively (see Fig. 1) [22–26]. Therefore, intense plastic straining induces the appearance of DSA and affects type of the PLC effect.

3.3. Fractography after tension

Transgranular dimple rupture is the main fracture mode observed for both material conditions (see Fig. 2). However, there is a difference in the sizes of the dimples and their distribution on the fracture surface. In the AA5083ZrHA1 alloy at $\varepsilon \sim 1$, very fine dimples having a well-defined conical shape were observed on the fracture surface (see Fig. 2a). No secondary phase particles were observed on the bottom of these dimples. The fracture surface does not change significantly with number pressing up to $\varepsilon \sim 4$. At $\varepsilon \sim 12$, a non-uniform distribution of dimple sizes was observed (see Fig. 2b). Coarse and deep dimples alternated with very fine dimples, indicating the activation of a limited number of nucleation sites. In the samples subjected to extensive deformation, the adjacent microvoids may coalesce and grow to a larger size in some areas. However, the overall grain matrix remained ductile.

In the AA5083ZrHA2 alloy at $\varepsilon \sim 1$, the fracture surface exhibits various dimple sizes (see Fig. 2c). An increase in the number of pressings (in this case to 4) resulted in an increase in the amount of non-uniformities. A minor portion of the coarse microvoids nucleate at the grain boundaries (see Fig. 2d). However, transgranular rupture is the dominant facture characteristic. At $\varepsilon \sim 12$, the coarse particles of the secondary phases are observed on the bottom of the conically shaped coarse dimples (see Fig. 2e). It is apparent that decohesion of coarse particles initiates microvoid coalescence and leads to the formation of conically shaped coarse dimples. Thus, the effect of ECAP on the fracture behavior under tension is insignificant. The material for both conditions remains ductile after any prior processing. Therefore, the ductility of the AA5083Zr alloy in both conditions is attributed to strain hardening behavior.

4. Discussion

Inspection of the experimental results showed than an increase in the YS of the AA5083Zr alloy due to the intense plastic straining could be associated with the three mechanisms that contribute to
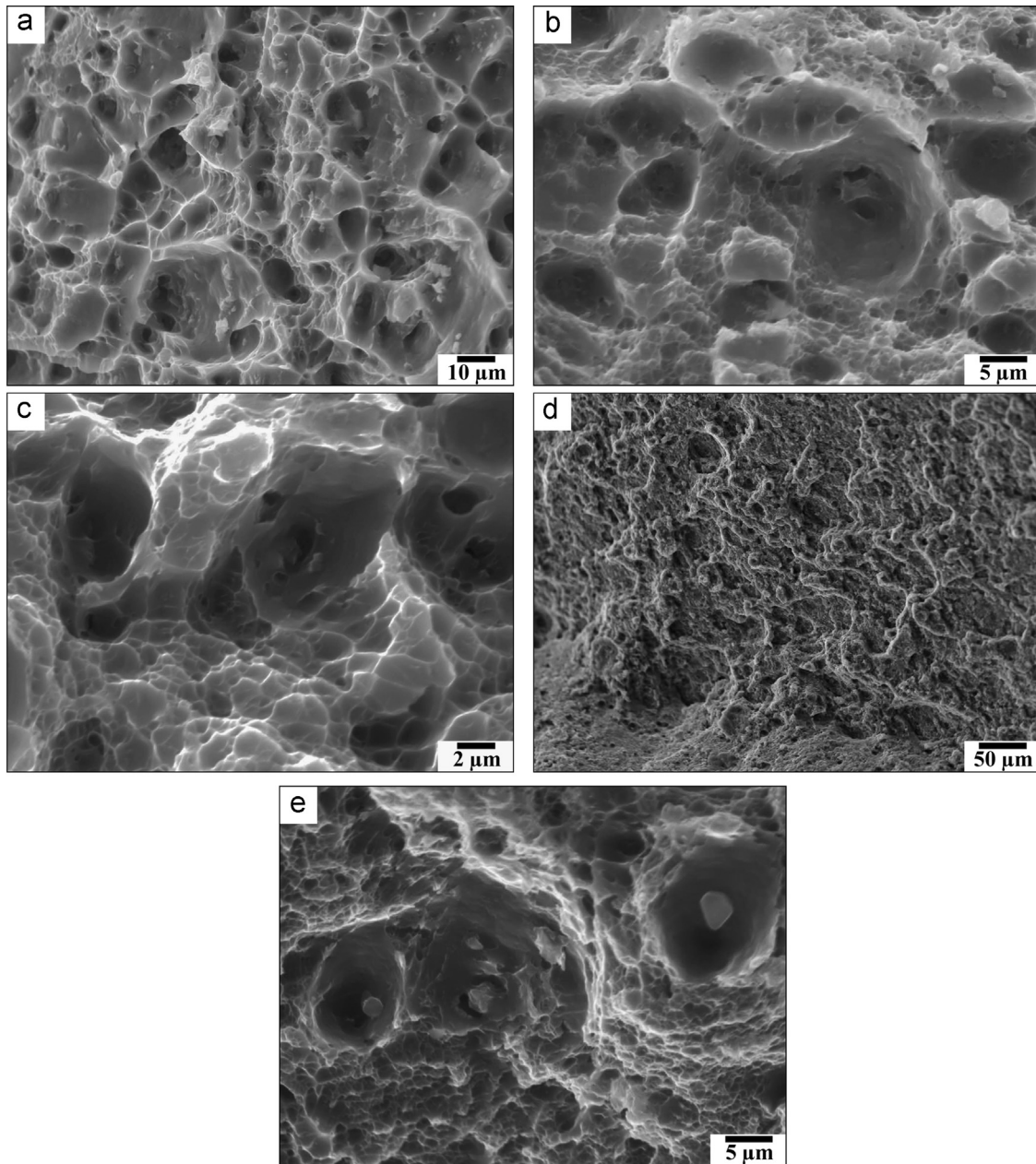
Fig. 2. SEM micrographs illustrating the fracture surfaces of tensile specimens: AA5083ZrHA1 exposed to (a) 1 and (b) 12 ECAP passes and AA5083ZrHA2 exposed to (c) 1, (d) 4 and (e) ECAP 12 passes, respectively.

the overall strength: (i) grain boundary strengthening, which is related to the distance between the HABs or LABs for moderate degrees of misorientation [21], which are impenetrable obstacles to gliding dislocations, (ii) dislocation strengthening related to the high dislocation density within grains and (sub)grains and (iii) a type of solid solution hardening related to DSA [22–27]. Dispersion hardening is not related to the increase in the YS because ECAP was not found to have any effect on the dispersions of the secondary phases (see Tables 1 and 2). However, the dispersion of the Al_6Mn phase affects the contribution of the aforementioned strengthening mechanisms on the overall YS of the AA5083Zr alloy after pressing.

It is assumed that these strength contributions are linearly additive [21,28]. Therefore, the total YS of the AA5083Zr alloy for the two different conditions can be expressed as

$$\sigma = \sigma_0 + \sigma_p + \sigma_{DSA} + \sigma_d + \sigma_{GB}, \tag{2}$$

where σ_0 is the resistance to dislocation glide within grains, σ_p is the dispersion strengthening, σ_d is the deformation strengthening, σ_{GB} is grain boundary strengthening and σ_{DSA} is additional frictional resistance due to DSA. The contributions from these strengthening mechanisms will be analyzed separately.

In Al–Mg alloys, the friction resistance is believed to be dominated by a general type of solid solution strengthening that is attributed to the interaction between mobile dislocations and stationary solute atoms [29]. This first type of solid solution strengthening is controlled by the magnesium solute content, which is estimated to be $\sim$100 MPa for $\sim$5 wt% Mg at ambient temperatures [29,30]. In this study, no evidence was observed to indicate the precipitation of the Mg-containing second-phase particles during ECAP. Therefore, σ_0 is independent of the number of pressings provides no contribution to the increase in the YS with additional strain (see Tables 5 and 6). It is worth noting that the Mn solute atoms may also contribute to the solid solution

strengthening [29]. However, the volume fraction of the Al_6Mn phase (see Table 1) is indicative of a very small portion of the Mn solute being retained in the aluminum solid solution, as is very little as observed in other Al–Mg–Mn alloys [30]. Thus, the effect of the Mn solute on the solid solution strengthening was disregarded.

The majority of the Mn content in the AA5083 alloy for both conditions is contained within the precipitates at the incoherent interfaces that act as obstacles to dislocation motion [29]. The precipitation strengthening is associated only with Orowan bowing and can be estimated from [30]

$$\sigma_p = (3.1)(0.84)Gb/\lambda, \tag{3}$$

where λ is the inter-particle spacing. The contribution of dispersion hardening associated with the plate-like shaped Al_6Mn particles in the AA5083ZrHA2 alloy is very small (see Table 6). In the AA5083ZrHA1 alloy, the contribution of dispersion hardening associated with the Al_6Mn nanoscale dispersoids having round shape is higher by a factor of ~ 4 (see Table 5). However, this σ_p value is low compared to the contributions from the other strengthening mechanisms in accordance with Eq. (2).

The contribution of the second type of solid solution strengthening mechanism, which is associated with the formation of clusters of Mg solute atoms on the lattice dislocations that requires extra force to ensure dislocation glide, was calculated using the approach described by Kang et al. [27]. The solid solution strengthening contribution from the DSA is considered to be equal to the stress drop size on the stress–strain curves

$$\sigma_{DSA} \approx \sigma_{drop}, \tag{4}$$

where σ_{drop} is a maximum drop stress observed on the stress–strain curve (see Fig. 1). This contribution was taken into account only after 2, 4, 8 and 12 ECAP passes because no DSA phenomenon were observed in the initial material conditions and after the first pressing. The results in Tables 5 and 6 show that the DSA contribution to the overall strength is negligible.

The conventional Hall–Petch relationship used to describe grain-boundary strengthening was

$$\sigma_{GB} = k_y d_{GB}^{-1/2}, \tag{5}$$

where d_G denotes the mean grain size. In the present calculations, the authors used all the HABs and d_G was calculated to be the average distance between any HABs. The Hall–Petch slope, k_y [11] was found to be 0.22 MPa $m^{1/2}$ for all the material conditions (see Fig. 3). Therefore, the dispersion of Al_6Mn-phase has no effect on the sensitivity of the YS to the grain size. Tables 5 and 6 show that grain size strengthening plays a major role in the increase of the YS at strains of $\varepsilon > 4$ for both material conditions. For the AA5083ZrHA1 alloy, the grain size strengthening is greater than for the other material condition at $\varepsilon > 2$. Therefore, a fine dispersion of Al_6Mn nanoscale dispersoids promoting grain refinement [18] allows a greater YS to be obtained for the AA5083Zr alloy using ECAP.

The dislocation strengthening is described by [21,31]

$$\sigma_d = M\alpha Gb\rho^{1/2}, \tag{6}$$

where ρ is dislocation forest density (Tables 1 and 2). During intense plastic deformation at low temperature in aluminum alloys, the microstructure separated into crystallites at LABs that may also contribute to dislocation strengthening. Based on this, an expanded version of Eq. (6) was written as [21]

$$\sigma_d = M\alpha Gb(\rho_o + \rho_{LABs})^{1/2}, \tag{7}$$

where M is the average Taylor factor from the texture data (taken to be 3.06 for a random texture), α is a constant (≈ 0.24), G is the shear modulus of aluminum (25,400 MPa), b is the Burgers vector (0.286 nm), ρ_o is dislocation forest density (see Tables 1 and 2) and ρ_{LABs} is the dislocation density stored in the LABs, which are capable of being penetrated by gliding dislocations [3,24,29]. The ρ_{LABs} values were calculated using [3,21,31]

$$\rho_{LABs} = \frac{3\theta_{LABs}}{bd_{LABs}}, \tag{8}$$

where θ_{LABs} is the misorientation of the aforementioned dislocation boundaries ($\sim 1.7°$), d_{LABs} is the average distance between the LABs with an average misorientation of $< 2°$ and $2–3°$, which are calculated from the TEM and EBSD data, respectively [18], and added together [29]. Finally, the deformation strengthening was calculated separately using Eq. (6) by taking into account only the

Table 5
Contribution of strengthening mechanisms in the AA5083ZrHA1.

Material condition	Calculated strengthening (MPa)						Experimental yield stress (MPa)
	Solid-solution	Precipitation	DSA	Dislocation	Grain-boundary	Total	
HA1	100	8	–	5	14	127	125
ECAP 1 pass	100	8	–	**61** (146)	**19** (91)	**187** (345)	180
ECAP 2 passes	100	8	7	**58** (145)	**28** (110)	**202** (371)	200
ECAP 4 passes	100	8	13	**65** (148)	**53** (180)	**240** (449)	230
ECAP 8 passes	100	9	16	**48** (141)	**127** (201)	**300** (467)	285
ECAP 12 passes	100	9	25	**47** (141)	**180** (220)	**361** (495)	335

Table 6
Contribution of strengthening mechanisms in the AA5083ZrHA2.

| Material condition	Calculated strengthening (MPa)						Experimental yield stress (MPa)
	Solid-solution	Precipitation	DSA	Dislocation	Grain-boundary	Total	
HA2	100	2	–	5	14	121	125
ECAP 1 pass	100	2	–	**37** (153)	**19** (90)	**158** (345)	160
ECAP 2 passes	100	2	5	**36** (153)	**29** (86)	**172** (346)	185
ECAP 4 passes	100	2	13	**33** (152)	**43** (156)	**191** (423)	220
ECAP 8 passes	100	2	18	**33** (152)	**83** (164)	**236** (436)	255
ECAP 12 passes	100	2	26	**33** (152)	**116** (169)	**277** (449)	270
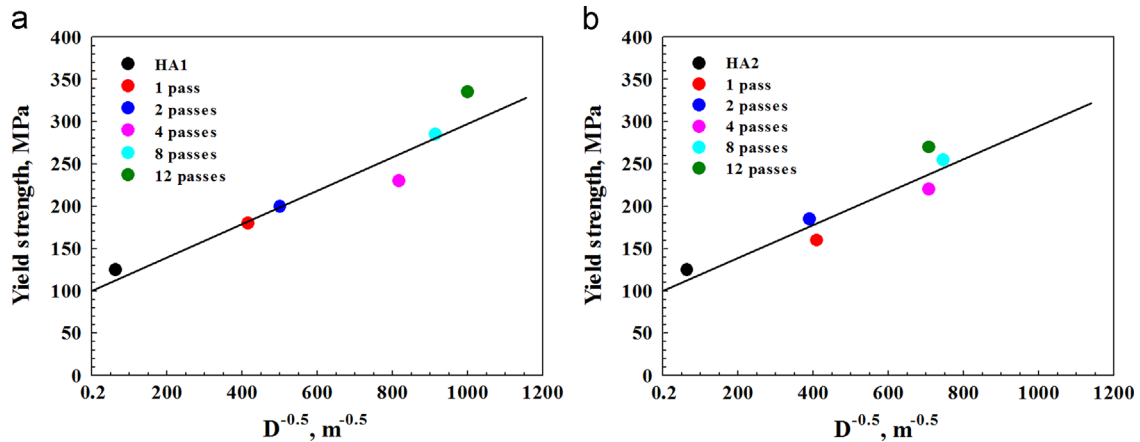
Fig. 3. Experimental yield strength-boundary spacing relationship for (a) the AA5083ZrHA1 and (b) the AA5083ZrHA2 under different conditions.

forest dislocation density and using Eq. (7) by taking into account both the forest dislocation density and the density of dislocations stored in the LABs with a misorientation of $\leq 3°$. Tables 5 and 6 show that the last approach (the conformable values are presented in brackets) gave an overestimation for both material conditions and Eq. (6) provided a good match between the calculation and the experiments. Therefore, there is a significant difference between the role of LABs with a low misorientation induced by warm deformation and cold deformation [21,31]. This difference was caused by the fact that during warm working, the deformation-induced LABs easily acquire a regular dislocation structure through dislocation short-range climbing [32] and could be considered to be sub-boundaries [18]. This process eliminates or highly decreased the long-range stress fields that originate from these boundaries [18,32]. As a result, deformation-induced sub-boundaries cannot contribute to deformation strengthening. In contrast, during cold working [21,31], the deformation-induced LABs retain their irregular dislocation structure and the long-range stress fields provide a significant contribution to the overall dislocation strengthening. Tables 5 and 6 show that deformation strengthening associated with the forest dislocation density plays a major role in the increase of the YS during the first and second ECAP pressings. For the AA5083ZrHA1 alloy, Al_6Mn nanoscale dispersoids promote the accumulation of the high dislocation density and, therefore, increased contribution of deformation strengthening to overall YS (Tables 1 and 2) [18].

It was shown [21] that LABs with misorientation angles greater than 3° act as conventional grain boundaries in terms of their strength contribution. To evaluate the effect of sub-boundary formation on the YS, the grain boundary strengthening originating from these LABs was calculated using Eq. (5), in which d_{GB} was taken to be the mean distance between any boundaries with a misorientation $\geq 3°$. These d_{GB} values were taken from the misorientation maps [18] (see Tables 1 and 2 where the conformable values are presented in brackets). The calculations based on this well adopted concept [21] provide a distinct overestimation based on the experimental data (see Tables 5 and 6 where the conformable values are presented in brackets). The overestimated values of the grain boundary strengthening indicates that the LABs with misorientations greater than or less than 3° do not contribute to this type of strengthening [21,31]. It is obvious that this is the other important difference between LABs induced by deformation at room temperature in Al [21] and at 300 °C in the AA5083Zr alloy [18] from a mechanical behavior point of view. It appeared that sub-boundaries containing even moderate amounts of misorientation within the regular dislocation structure [18] are essentially transparent to gliding dislocations.

Thus, in the AA5083Zr alloy, the increase in the YS resulting from ECAP at an intermediate temperature was caused by the formation of new HABs and the increase in the dislocation density within sub-grains and/or grains. In contrast in the aluminum [21] and Al–Mg alloys [5–9] subjected to intense plastic straining at low temperatures the increase in the YS is attributed to the formation of new boundaries with misorientations $\geq 3°$. Cold working results in the formation of LABs with irregular dislocation structures in Al–Mg alloys [16], and these boundaries can contribute to deformation strengthening and grain size strengthening, concurrently. This is why the YS values of the AA5083Zr alloy subjected to ECAP at 300 °C over both conditions were slightly less than that of the Al–Mg alloy subjected to ECAP at temperatures ranging from 20 to 200 °C despite a higher Mg content [3–9]. Therefore, for cold worked aluminum alloys, the exact characteristics of the deformation-induced boundary assembly are not so important to the determination of mechanical properties. Cold working provides greater increases to the YS for Al–Mg alloys [14,15] that can be predicted from the Hall–Petch relationship due to the fact that deformation-induced LABs play an important role in strengthening. Warm working provides a moderate increase to the YS because only HABs and forest dislocations can contribute to the overall increase in the strength. However, the ductility of the warm-worked alloy was two to three times higher than cold-worked alloys [3–9]. Therefore, the Al–Mg–Zr alloy subjected to extensive warm working provides a balanced combination of strength and ductility [33]. The optimization of the dispersion of secondary phase particles may increase the YS resulting from a warm ECAP process.

5. Conclusions

In this work, we examined the effect of extensive grain refinement on the mechanical properties of a Zr-modified 5083 aluminum alloy that was subjected to two different types of homogenization annealing followed by ECAP at 300 °C at strains of up to $\varepsilon \sim 12$. The primary conclusions from this work can be summarized as follows:

1) ECAP at 300 °C and $\varepsilon \sim 12$ for an alloy containing a nanoscale Al_6Mn dispersoids provided an increase of 168% and 48% to the YS and UTS, respectively, due to the extensive grain refinement. The effect of the same processing on the properties of the alloy containing coarse, plate-like shaped Al_6Mn particles resulted in an increase of 116% and 23% for the YS and UTS, respectively. Both alloys exhibited high ductility.

2) The Hall–Petch analysis showed that grain size strengthening corresponding to a slope of $k_y \approx 0.22$ MPa m$^{1/2}$ played a major role in the strengthening provided by ECAP after 4 passes. At moderate strains, the deformation strengthening is the main contributor to the overall increase in strength.

3) Increases in the strength of the alloy as a result of the ECAP process were attributed to the formation of high-angle grain boundaries and forest dislocations within the grains and sub-grains. No effect was observed from deformation-induced sub-boundaries for either boundary or dislocation strengthening.

Acknowledgments

References

[1] I.J. Polmear, Light Alloys. From Traditional Alloys to Nanocrystals, 4th ed., Butterworth-Heinemann/Elsevier, UK, 2006.
[2] Smithells Light Metals Handbook, in: E.A. Brandes, G.B. Brook (Eds.), Butterworth-Heinemann, Oxford, 1998.
[3] I. Sabirov, M.Yu. Murashkin, R.Z. Valiev, Mater. Sci. Eng. A 560 (2013) 1–24.
[4] R.Z. Valiev, T.G. Langdon, Prog. Mater. Sci. 51 (2006) 881–981.
[5] K.-T. Park, J.H. Park, Y.Sh. Lee, W.J. Nam, Mater. Sci. Eng. A 408 (2005) 102–109.
[6] T.L. Tsai, P.L. Sun, P.W. Kao, C.P. Chang, Mater. Sci. Eng. A 342 (2003) 144–151.
[7] M.A. Munoz-Morris, C. Garsia Oca, D.G. Morris, Scr. Mater. 48 (2003) 213–218.
[8] R. Kapoor, J.K. Chakravartty, Acta Mater. 55 (2007) 5408–5418.
[9] J. Gubicza, N.Q. Chinh, T. Csanadi, T.G. Langdon, T. Ungar, Mater. Sci. Eng. A 462 (2007) 86–90.
[10] M. Furukawa, Z. Horita, M. Nemoto, R.Z. Valiev, T.G. Langdon, Philos. Mag. 78 (1998) 203–215.
[11] R.Z Valiev, Mater. Trans. 55 (2014) 13–18.
[12] D.J. Lloyd, S.A. Court, Mater. Sci. Technol. 19 (2003) 1349–1354.
[13] H. Hasegawa, S. Komura, A. Utsunomiya, Z. Horita, M. Furukawa, M. Nemoto, et al., Mater. Sci. Eng. A 265 (1999) 188–196.
[14] R.Z. Valiev, N.A. Enikeev, M.Yu. Murashkin, V.U. Kazykhanov, X. Sauvage, Scr. Mater. 63 (2010) 949–952.
[15] P.V. Liddicoat, X.-Z. Liao, Y. Zhao, Y. Zhu, M.Y. Murashkin, E.J. Lavernia, R.Z. Valiev, S.P. Ringer, Nat. Commun. 1 (2010) 1–7.
[16] D.G. Morris, M.A. Munoz-Morris, Acta Mater. 50 (2002) 4047–4060.
[17] J.S. Hayes, R. Keyte, P.B. Prangnell, Mater. Sci. Technol. 16 (2000) 1259–1263.
[18] I. Nikulin, A. Kipelova, S. Malopheyev, R. Kaibyshev, Acta Mater. 60 (2012) 487–497.
[19] F.J. Humphreys, M. Hatherly, Recrystallization and Related Annealing Phenomena, Elsevier, Oxford, 2005.
[20] H.W. Zhang, X. Huang, R. Pippan, N. Hansen, Acta Mater. 58 (2010) 1698–1707.
[21] N. Kamikawa, X. Huang, N. Tsuji, N. Hansen, Acta Mater. 57 (2009) 4198–4208.
[22] M.A. Lebyodkin, N.P. Kobelev, Y. Bougherira, D. Entemeyer, C. Fressengeas, V.S. Gornakov, T.A. Lebedkina, I.V. Shashkov, Acta Mater. 60 (2012) 3729–3740.
[23] H. Halim, D.S. Wilkinson, M. Niewczas, Acta Mater. 55 (2007) 4151–4160.
[24] I.V. Shashkov, M.A. Lebyodkin, T.A. Lebedkina, Acta Mater. 60 (2012) 6842–6850.
[25] Y. Brechet, Y. Estrin, Acta Metall. Mater. 43 (1995) 955–963.
[26] J.M. Robinson, M.P. Shaw, Int. Mater. Rev. 39 (1994) 113–121.
[27] J. Kang, R.K. Mishra, D.S. Wilkinson, O.S. Hopperstad, Philos. Mag. Lett. 92 (2012) 647–655.
[28] X. Zhang, A. Godfrey, X. Huang, N. Hansen, Q. Liu, Acta Mater. 59 (2011) 3422–3430.
[29] E.L. Huskins, B. Cao, K.T. Ramesh, Mater. Sci. Eng. A 527 (2010) 1292–1298.
[30] K.L. Kendig, D.B. Miracle, Acta Mater. 50 (2002) 4165–4175.
[31] A.A. Gazdera, W. Cao, Ch.H.J. Davies, E.V. Pereloma, Mater. Sci. Eng. A 497 (2008) 341–352.
[32] A. Belyakov, T. Sakai, R. Kaibyshev, Metall. Mater. Trans. 29 (1998) 161–167.
[33] A. Magee, L. Ladani, T.D. Topping, E.J. Lavernia, Acta Mater. 60 (2012) 5838–5849.